

Terahertz Pulse Generation by Strongly Magnetized, Laser-Created Plasmas

C. Tailliez,^{*} X. Davoine, A. Debayle, L. Gremillet[✉], and L. Bergé[✉]

CEA, DAM, DIF, F-91297 Arpajon, France and Université Paris-Saclay, CEA, LMCE, 91680 Bruyères-le-Châtel, France

 (Received 5 November 2021; revised 26 January 2022; accepted 7 March 2022; published 29 April 2022)

Relativistic interactions between ultraintense ($>10^{18}$ W cm⁻²) laser pulses and magnetized underdense plasmas are known to produce few-cycle Cerenkov wake radiation in the terahertz (THz) domain. Using multidimensional particle-in-cell simulations, we demonstrate the possibility of generating high-field (>100 GV m⁻¹) THz bursts from helium gas plasmas embedded in strong (>100 T) magnetic fields perpendicular to the laser path. We show that two criteria must be satisfied for efficient THz generation. First, the plasma density should be adjusted to the laser pulse duration for a strong resonant excitation of the electromagnetic plasma wake. Second, in order to mitigate the damping of the transverse wake component across the density gradients at the plasma exit, the ratio of the relativistic electron cyclotron and plasma frequencies must be chosen slightly above unity, but not too large, lest the wake be degraded. Such conditions lead the outgoing THz wave to surpass in amplitude the electrostatic wakefield induced in a similar, yet unmagnetized plasma.

DOI: [10.1103/PhysRevLett.128.174802](https://doi.org/10.1103/PhysRevLett.128.174802)

Terahertz (THz) radiation sources are employed in many technological fields, including cancer detection [1] and material identification [2]. Some rapidly emerging applications specifically require high (\sim GV m⁻¹) field strengths, e.g., to diagnose the dynamics of water molecules [3], induce rapid phase transitions [4], or for atom probe tomography [5]. A standard technique to produce relatively energetic (\sim 10 μ J) THz pulses makes use of laser optical rectification in nonlinear crystals [6]. Another consists of focusing two laser harmonics into a gas plasma, leading to THz pulse energies up to \sim 0.2 mJ with mid-IR laser drivers [7–9]. More energetic THz bursts, approaching the mJ level, can be attained in relativistic laser-matter interactions [10–13].

To further increase the efficiency of THz sources using intense lasers, an external magnetic field may be applied to gas targets [14–16]. For B -field strengths of $B_0 \simeq 10$ –100 T, the electron cyclotron frequency $\omega_{ce} \equiv eB_0/m_e$ (m_e is the electron mass and e the elementary charge) lies in the 1–10 THz range, and thus directly impacts the THz spectrum. While ≤ 100 T B fields can be readily produced [17–19], nondestructive electromagnetic flux compression techniques [20,21] or kJ laser irradiation of capacitor-coil targets [22,23] nowadays deliver nanosecond magnetic pulses at the 1000 T level, which can be assumed static relative to the femtosecond timescales of THz radiation.

Applying a B field parallel to the laser propagation axis enables the THz emission spectrum and polarization state to be tuned, yet with limited leverage on the energy yield [15,16,24–28]. By contrast, a transversely magnetized plasma can allow intense short pulses to resonantly excite electromagnetic plasma wakefields [29], the transverse

component of which can be transmitted into vacuum through Cerenkov wake radiation (CWR) [14,30,31]. The wakefield then corresponds to the lower branch of the extraordinary (XO) plasma mode, driven at near the electron plasma frequency $\omega_{pe} = (n_e e^2 / \epsilon_0 m_e)^{1/2}$ (n_e is the electron density and ϵ_0 the vacuum permittivity). The radiation frequency is determined by the resonance condition $\omega/k = V_d \cos \theta$, where $V_d \simeq c$ is the group velocity of the laser driver, and ω and k are the frequency and wave number of the XO mode propagating at an angle θ relative to the laser direction.

In the linear limit, this mode verifies the dispersion relation $k^2 c^2 = \omega^2 - \omega_{pe}^2 (\omega^2 - \omega_{pe}^2) / (\omega^2 - \omega_H^2)$, where $\omega_H \equiv (\omega_{pe}^2 + \omega_{ce}^2)^{1/2}$ is the upper hybrid frequency. In the relativistic regime, Hu *et al.* [32] derived a simple relationship between the longitudinal (E_x) and transverse (E_\perp) electric field components for a 1D plasma wake:

$$E_\perp = b \frac{c}{\omega_{pe}} \partial_\xi E_x, \quad (1)$$

where $b \equiv \omega_{ce} / \omega_{pe}$ and $\xi = x - ct$. Validated against particle-in-cell (PIC) simulations in the plasma blowout regime at $b \ll 1$ [33], this formula supplies the expression

$$\mathcal{E}_\perp = b \mathcal{E}_x (1 + \bar{\mathcal{E}}_x^2 / 2) (1 + \bar{\mathcal{E}}_x^2 / 4)^{1/2}, \quad (2)$$

between the peak-to-peak longitudinal (\mathcal{E}_x) and transverse (\mathcal{E}_\perp) field amplitudes ($\bar{\mathcal{E}}_x = e \mathcal{E}_x / m_e \omega_{pe} c$), which recovers the standard relation $\mathcal{E}_\perp / \mathcal{E}_x = b$ in the linear limit [34].

An important practical issue is whether the transverse wake component can be efficiently transmitted into the

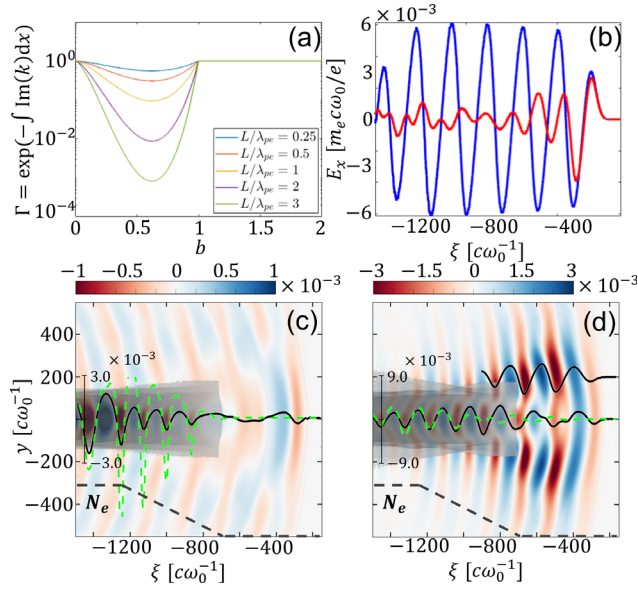


FIG. 1. (a) Damping coefficient (Γ) of the CWR through a linear density down-ramp as a function of b , for different values of the normalized gradient length L/λ_{pe} [35]. (b),(c),(d) 2D PIC simulations of the CWR induced by a laser pulse with $a_0 = 0.8$ in a magnetized He plasma with $n_e = 1.11 \times 10^{18} \text{ cm}^{-3}$ ($\nu_{pe} = 10 \text{ THz}$). (b) On-axis lineouts of the longitudinal (E_x) wakefields (inside plasma) corresponding to panels (c) (blue curve) and (d) (red curve). (c),(d) 2D maps of the transverse (E_z) THz fields when the laser has left the plasma: (c) $B_0 = 179 \text{ T}$ ($\nu_{ce} = 5 \text{ THz}$, $b = 0.5$); (d) $B_0 = 537 \text{ T}$ ($\nu_{ce} = 15 \text{ THz}$, $b = 1.5$). Black curves are lineouts of the THz E_z fields, on axis or at $y = 200c/\omega_0$; green curves are computed from the on-axis E_x field using Eq. (1). Gray areas represent plasma electron density profiles. Black dashed lines indicate the initial He density profile with $L = 95 \mu\text{m}$ ($L/\lambda_{pe} = 3$). Electric fields are shown in units of $m_e c \omega_0 / e \approx 3.21 \times 10^{12} \text{ V m}^{-1}$.

vacuum. In a realistic setting, the plasma-vacuum boundary has a finite gradient length, typically larger than $\lambda_{pe} = 2\pi c/\omega_{pe}$, through which the excited wave may turn evanescent between the lower and upper branches of the local XO modes. Within linear theory, the damping coefficient is given by $\Gamma = \exp[-\int \text{Im}(k)(x) dx]$ [14]. Taking $\omega_{pe}^2 \rightarrow \omega_{pe}^2(1-x/L)$, one can compute Γ as a function of the magnetization parameter b and the normalized density scale length L/λ_{pe} , as plotted in Fig. 1(a). It appears that damping only occurs for $b < 1$ and increases with L (see also Supplemental Material [35]).

The above considerations suggest that operating at $b > 1$ values should enable the transverse component of the wake to be dominant and fully transmitted outside the plasma. Surprisingly, this strongly magnetized interaction regime has never been investigated previously, except in Ref. [38], which only addressed *in situ* properties of 1D wakes and did not characterize the outgoing THz waves. In this Letter, for the first time, we examine via multidimensional PIC simulations the changes brought to the electromagnetic

wake and associated THz radiation driven by an intense laser pulse in a strongly magnetized plasma. We demonstrate that provided the resonance condition for the wakefield excitation is satisfied, the outgoing THz radiation is given a strong boost when $b \gtrsim (1 + a_0^2/4)^{1/4}$ ($a_0 \equiv eE_0/m_e c \omega_0$ is the dimensionless laser field strength and ω_0 the laser frequency), both in terms of THz wave amplitude ($>100 \text{ GV m}^{-1}$) and laser-to-THz energy conversion efficiency ($>10^{-3}$). This optimum magnetization range results from a tradeoff between efficient generation and transmission of the transverse wakefield.

Simulations are performed with the PIC CALDER code [11,39] that solves the relativistic Vlasov-Maxwell equations together with strong-field ionization [40] in 2D3V geometry (2D in space and 3D in momentum). The longitudinal (transverse) axis is set along x (resp. y), while the laser pulse is linearly polarized in the (out-of-plane) z direction. The laser pulse, of wavelength $\lambda_0 = 1 \mu\text{m}$, is Gaussian in space and time, with $w_0 = 10.5 \mu\text{m}$ FWHM transverse width, $\tau_0 = 35 \text{ fs}$ FWHM duration, and a field strength a_0 in the range $0.8 \leq a_0 \leq 16$. The round shape of the pulse ($c\tau_0 \approx w_0 \sim \sqrt{a_0}c/\omega_{pe}$) favors wake excitation in the blowout regime ($a_0 > 1$) [41]. In the laser's comoving coordinates ($\xi = x - ct$, $\tau = t$), the pulse maximum is located at $\xi = -300 \mu\text{m}$. The pulse is focused into a helium gas target with an electron plasma frequency lying in the range $4 \leq \nu_{pe} \equiv \omega_{pe}/2\pi \leq 10 \text{ THz}$ at full ionization, and a trapezoidal density profile with varying ramp lengths (L). Open boundary conditions are used in all directions for both particles and fields. A static and uniform magnetic field $\vec{B}_0 = B_0 \vec{e}_y$ permeates the plasma, with field strength $B_0 \in (179, 286, 572) \text{ T}$ corresponding to cyclotron frequencies $\nu_{ce} \equiv \omega_{ce}/2\pi \in (5, 8, 16) \text{ THz}$. The THz signal is extracted by Fourier filtering the E_z field (i.e., the dominant component of the THz field, elliptically polarized perpendicularly to \vec{k} [35]) with an upper cutoff frequency $\nu_{co} = \omega_{co}/2\pi = 90 \text{ THz}$.

We start by considering the weakly relativistic regime ($a_0 = 0.8$) at the plasma frequency $\nu_{pe} = 10 \text{ THz}$ and density scale length $L/\lambda_{pe} = 3$. Figures 1(c) and 1(d) display 2D maps of the transverse (E_z) THz field for two magnetization levels, shortly after the laser pulse has left the plasma region (gray areas). For $\nu_{ce} = 5 \text{ THz}$ ($b = 0.5$) [Fig. 1(c)], the E_z wakefield reaches $\approx 3 \times 10^{-3} m_e \omega_0 c / e$, i.e., about half the strength of the E_x wakefield component [compare the on-axis lineout of E_z and Fig. 1(b)]. It is significantly damped ($\Gamma \approx 0.2$) across the down-ramp, albeit less than predicted by linear theory [$\Gamma \approx 1.4 \times 10^{-3}$, see Fig. 1(a)]. This behavior is dramatically altered when raising the magnetization to $b = 1.5$ [Fig. 1(d)]: the plasma wake becomes dominantly transverse and its on-axis E_z component, driven in the plasma ($\xi < -1200c\omega_0^{-1}$) to 1.7 times the E_x wakefield amplitude, is now negligibly attenuated across the plasma

boundary. Hence, a wave packet of $\sim 10 \text{ GV m}^{-1}$ amplitude is radiated into the vacuum.

Several other features are worth noting. First, the longitudinal wake excited in the plasma turns strongly anharmonic and fast-decaying for $b > 1$, as shown in Fig. 1(b) and already reported in [38,42]. Moreover, although our simulations are 2D, the dependence between E_{\perp} and E_x is well captured by Hu's 1D formula (1), both at $b = 0.5$ and $b = 1.5$ [43]. This is illustrated in Figs. 1(c) and 1(d), in which the E_z lineouts computed from Eq. (1) (dashed green curves) along the plasma plateau reasonably agree with their counterparts extracted from the simulations (solid black curves). Lastly, the THz emission at $b = 1.5$ peaks at nonzero ($\sim \pm 16^\circ$) angles to the laser path, resulting in the $\simeq 3.5m_e c \omega_0 / e$ field maxima seen at $y \simeq \pm 200c/\omega_0$ in Fig. 1(b). This may originate from diffraction due to the finite width of the plasma channel together with the enhanced off-axis emission that is expected at higher b values [35].

We now investigate the relativistic regime by increasing the laser field strength to $a_0 = 4$. The nonlinear plasma wakefield here takes on a sawtooth shape, causing the $\partial_{\xi} E_x$ term of Eq. (1) to reach high local values. Figures 2(a)–2(d) show the transverse THz fields driven in a He gas of fixed electron density $n_e = 7.94 \times 10^{17} \text{ cm}^{-3}$ ($\nu_{pe} = 8 \text{ THz}$), rear-side gradient length $L = 200 \mu\text{m}$ ($L/\lambda_{pe} = 5.34$), and subject to a B field characterized by $\nu_{ce} = 8 \text{ THz}$ ($b = 1$) or 16 THz ($b = 2$). One can see that THz fields as strong as $\simeq 0.12m_e \omega_0 c / e$ (380 GV m^{-1}) and $\simeq 0.17m_e \omega_0 c / e$ (540 GV m^{-1}) are generated in the plasma when $b = 1$ and $b = 2$, respectively [Figs. 2(a) and 2(b)]. Again, their on-axis profile is well reproduced by Eq. (1). For $b = 1$, a single-cycle pulse, located at $\xi \simeq -550c/\omega_0$, escapes from the plasma with a $\simeq 0.02m_e c \omega_0 / e$ amplitude. For $b = 2$, by contrast, although diffraction causes the on-axis fields to decrease, a train of twice stronger ($\simeq 0.05m_e \omega_0 c / e$) pulses are emitted obliquely into vacuum [Fig. 2(d)].

Figures 2(e) and 2(f) display the spatial energy spectra (integrated over the transverse wave number, k_y) of the THz pulses against k_x , the longitudinal wave number. For $b = 1$, the fundamental component prevails in the plasma, but drops by 35% across the down ramp. This component also prevails for $b = 2$ and is even amplified when passing through the ramp [see Fig. 3(a)].

The condition for efficient transmission of the transverse wakefield thus appears to be more stringent at relativistic laser intensity. This is ascribed to the increased inertia of the plasma electrons oscillating in the large-amplitude wakefield. The above findings, however, indicate that it suffices to consider the fundamental frequency of the wake. Since the plasma and cyclotron frequencies associated with electrons of mean Lorentz factor γ become $\omega_{pe}/\sqrt{\gamma}$ and ω_{ce}/γ , respectively, substituting these expressions into the dispersion relation of the XO mode gives the generalized condition for full transmission, namely, $b \geq \sqrt{\gamma}$.

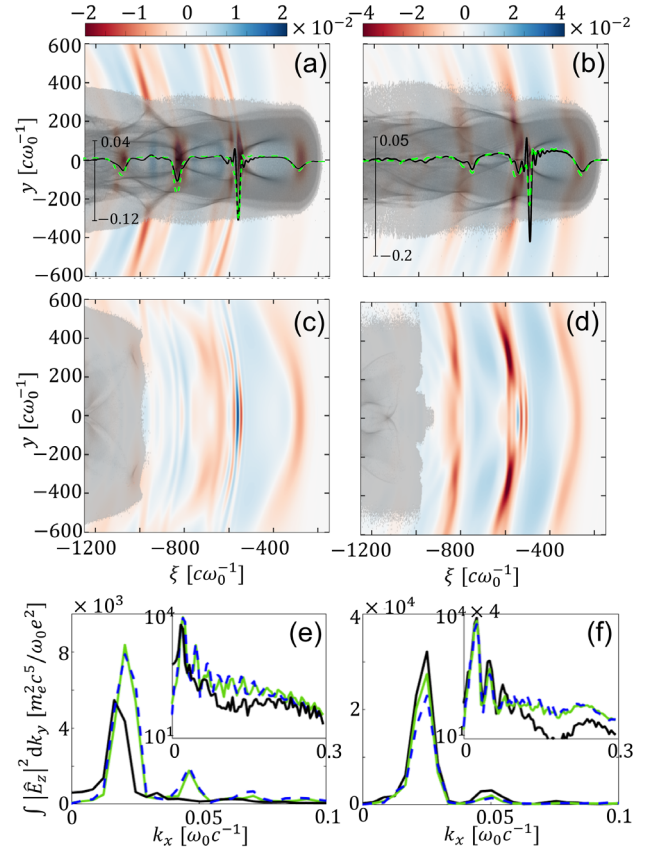


FIG. 2. THz E_z fields (a),(b) after $400 \mu\text{m}$ of propagation inside the plasma and (c),(d) after crossing a $200 \mu\text{m}$ -long plasma down-ramp, produced for $a_0 = 4$ in a magnetized He plasma with $n_e = 7.94 \times 10^{17} \text{ cm}^{-3}$ ($\nu_{pe} = 8 \text{ THz}$). In (a),(b), black and green curves plot on-axis lineouts of the simulated and reconstructed THz E_z fields using Eq. (1), respectively. Gray areas represent electron density profiles. (e),(f) Spatial energy spectra (integrated over the transverse wave number k_y) vs longitudinal wave number k_x , after $400 \mu\text{m}$ of propagation inside the plasma (blue dashed curves), after crossing a $200 \mu\text{m}$ -long plasma down-ramp (black curves) or after crossing a sharp plasma-vacuum boundary (green curves). Insets display the same spectra in \log_{10} scale. B_0 is such that $\nu_{ce} = 8 \text{ THz}$ ($b = 1$ and $\tilde{b} = 0.67$) in (a), (c),(e) and $\nu_{ce} = 16 \text{ THz}$ ($b = 2$ and $\tilde{b} = 1.34$) in (b),(d),(f).

An estimate for γ can be obtained from Eq. (2) together with $\mathcal{E}_z = b\beta_x/(1 - \beta_x) \simeq 2b\gamma^2$ ($\beta_x \equiv v_x/c \sim 1$ is the normalized electron velocity) [32]. Combining these two relations and approximating the longitudinal wakefield by $\mathcal{E}_x \sim en_e \sqrt{a_0} c / \omega_{pe} = \alpha \sqrt{a_0} m_e c \omega_{pe} / e$ (α is an *ad hoc* factor) [41] then yields $\gamma \approx \sqrt{1 + \alpha^4 a_0^2 / 8}$. Our simulations confirm this scaling with $\alpha \simeq 2^{1/4}$. Hence, the fundamental component ($\omega \simeq \omega_{pe} / \sqrt{\gamma}$) of the CWR should freely escape the plasma provided $\tilde{b} \equiv b / (1 + a_0^2 / 4)^{1/4} \gtrsim 1$.

To support this prediction, we have run several simulations with varying plasma density, magnetization, and ramp length. Figure 3(a) plots the time evolution of the laser-to-THz energy conversion efficiency

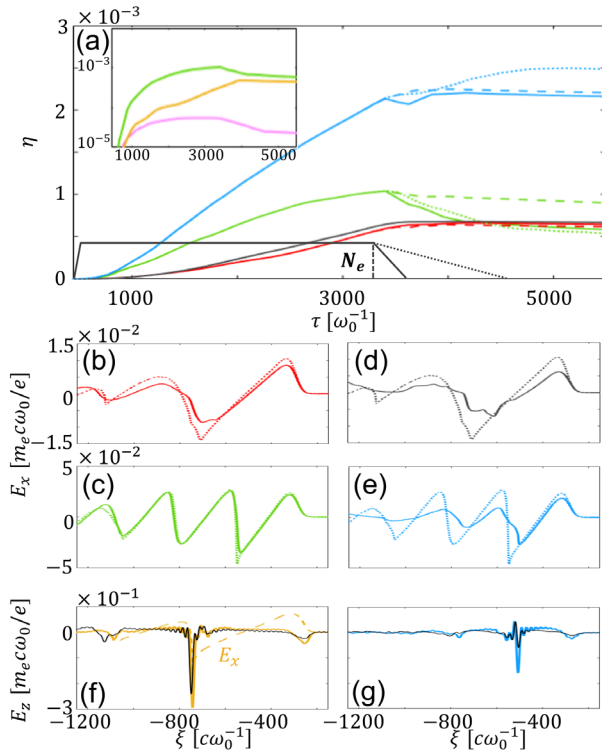


FIG. 3. (a) Laser-to-THz energy conversion efficiency versus time for various ν_{ce} and ν_{pe} values. Green, yellow, pink curves: $\nu_{ce} = \nu_{pe} = 8$ THz. Red curves: $\nu_{ce} = 8$ THz, $\nu_{pe} = 4$ THz. Blue curves: $\nu_{ce} = 16$ THz, $\nu_{pe} = 8$ THz. Gray curve: $\nu_{ce} = 16$ THz, $\nu_{pe} = 4$ THz. The laser field strength is $a_0 = 4$, except for the pink curve ($a_0 = 0.4$) and yellow curve ($a_0 = 16$) in the inset. Solid, dotted, and dashed curves correspond to $L = 50 \mu\text{m}$, $L = 200 \mu\text{m}$, and $L = 0 \mu\text{m}$, respectively. In (a), the trapezoid represents the electron density profile seen by the laser pulse. (b),(c),(d),(e) On-axis lineouts of the E_x wakefields in the plasma channel with (solid) and without (dotted curves) an external B field. The color code is the same as in (a). (f),(g) On-axis lineouts of the E_z fields inside the plasma (colored) and transmitted to vacuum (black curves).

$\eta \equiv \int |E_{\text{THz}}|^2 dx dy / \int |E_{\text{laser}}|^2 dx dy$, where E_{THz} denotes the low-frequency E_z field.

To start with, the inset of Fig. 3(a) visualizes, for $\nu_{ce} = \nu_{pe}$ and $L = 50 \mu\text{m}$, the nonlinear dependence of η on a_0 . A two orders of magnitude increase in η is obtained when passing from $a_0 = 0.4$ to $a_0 = 4$, which highlights the benefit of using relativistic laser pulses. Note, however, the clear decrease in the THz gain when $a_0 = 16$ (yellow curve), indicating the existence of an optimum laser intensity for given plasma parameters and pulse shape.

The best-performing setup is characterized by $\nu_{ce} = 16$ THz and $\nu_{pe} = 8$ THz (i.e., $\tilde{b} = 1.34$, see blue curve), which maximizes both the generation of the THz pulse inside the plasma and, for $L \leq 50 \mu\text{m}$, ensures its full transmission into vacuum, with a final conversion efficiency $\eta \simeq 2.2 \times 10^{-3}$. The corresponding E_x and E_z field

profiles are plotted in Figs. 3(e) and 3(g) after $400 \mu\text{m}$ of propagation in the plasma. The E_x wakefield becomes degraded compared to that excited in the unmagnetized plasma [dotted curve in Fig. 3(e)], and so the E_z wakefield mainly consists of a single cycle [Fig. 3(g)]. The ratio of the E_z and E_x amplitudes, $\mathcal{E}_z/\mathcal{E}_x \simeq 4.4$, is reasonably consistent with the prediction of Eq. (2), i.e., $\mathcal{E}_z/\mathcal{E}_x \approx 3$, taking $b = 2$ and $\bar{\mathcal{E}}_x = 0.85$. Notably, the THz transverse field greatly exceeds the longitudinal unmagnetized wakefield [compare Figs. 3(e) and 3(g)], and this hierarchy still holds after transmission into vacuum. For $L = 200 \mu\text{m}$ (blue dotted curve), the wakefield excitation is sustained in part of the down-ramp, leading to the enhanced fundamental component of the THz spectrum [Fig. 2(f)] and to a further increase in the radiated THz energy.

Considering again a $L = 50 \mu\text{m}$ ($1.33\lambda_{pe}$) down-ramp, lowering the cyclotron frequency to $\nu_{ce} = 8$ THz (green curve) weakens substantially both the generation (by $\simeq 55\%$) and transmission (by $\simeq 44\%$) of the THz wave packet, and hence the final THz yield plummets to $\eta \simeq 6 \times 10^{-4}$. Attenuation across the down-ramp follows from the effective magnetization parameter $\tilde{b} = 0.67$ dropping below unity. As expected, changing the density scale length to $L = 5.34\lambda_{pe}$ (dotted green curve) or 0 (dashed green curve) results in similar or almost no damping, respectively. Interestingly, Figs. 3(c) and 3(e) show that the longitudinal wakefield excited in the plasma is stronger at $\nu_{ce} = 8$ THz than at $\nu_{ce} = 16$ THz. However, in light of Eq. (2), this enhanced E_x wakefield does not compensate for the decrease in \tilde{b} , thereby diminishing the transmitted THz energy.

The red curve, associated with $\nu_{ce} = 8$ THz and $\nu_{pe} = 4$ THz, depicts another highly magnetized configuration ($\tilde{b} = 1.34$), but at reduced plasma density. Compared to the previous case, the larger magnetization only partly makes up for the weakened (by a factor of $\sim 2-3$) E_x wakefield that logically follows from the density decrease [Fig. 3(b)]. Yet the THz yield is fully transmitted as $\tilde{b} > 1$, and it approximately coincides with that achieved in the previous configuration. Notably, the radiation efficiency rises up to $\eta \simeq 1.5 \times 10^{-3}$ over 1.6 mm-long plasmas, due to cumulated lateral emissions [35]. Also, doubling the B -field strength ($\nu_{ce} = 16$ THz) while keeping $\nu_{pe} = 4$ THz ($\tilde{b} = 2.67$) further impairs the longitudinal wakefield [Fig. 3(d)], but the effect of this degradation on the fully transmitted THz field is counterbalanced by a higher $\mathcal{E}_z/\mathcal{E}_x$ ratio, giving the same final conversion efficiency [see gray and red curves in Fig. 3(a)].

Similar conclusions hold when the laser field is further intensified to $a_0 = 16$. At $\nu_{ce} = \nu_{pe} = 8$ THz, the THz E_z field is then about twice stronger than the E_x field [Fig. 3(f)], again fairly consistent with Eq. (2), while the THz pulse energy is fully transmitted through the boundary, due to the shortened effective gradient length

$L/\sqrt{\gamma}\lambda_{pe} \ll 1$. Yet the wakefield is driven far from the matching conditions [41] because the plasma density is kept constant, causing the conversion efficiency to dramatically drop (yellow curve in the inset).

In summary, our numerical simulations have revealed that laser-induced THz emissions from magnetized gas plasmas can be strongly enhanced when the ratio of the electron cyclotron to plasma frequencies verifies $\nu_{ce}/\nu_{pe} \gtrsim (1 + a_0^2/4)^{1/4}$. This criterion ensures that the transverse component of the excited wakefield dominates its longitudinal component and is fully transmitted into vacuum. Provided the condition of resonant wakefield excitation is approximately fulfilled, THz field strengths beyond 100 GV m^{-1} are predicted when focusing $\sim 10^{19} \text{ W cm}^{-2}$ femtosecond laser pulses into gas plasmas subject to $> 100 \text{ T}$ uniform B fields. These findings are of prime interest for the development of ultrahigh THz field sources and related applications.

The data that support the results of this study are available within the present Letter. Complementary data can be made available from the corresponding authors upon reasonable request.

We acknowledge the ‘‘Grand Equipement de Calcul Intensif’’ (GENCI) under the Grants No. A0070506129 and No. A0080507594, and the Agence Innovation D efense.

All authors contributed equally to this work.

* colomban.tailliez@cea.fr

- [1] M. Tonouchi, Cutting-edge terahertz technology, *Nat. Photonics* **1**, 97 (2007).
- [2] L. Berg e, K. Kaltenecker, S. Engelbrecht, A. Nguyen, S. Skupin, L. Merlat, B. Fischer, B. Zhou, I. Thiele, and P. U. Jepsen, Terahertz spectroscopy from air plasmas created by two-color femtosecond laser pulses: The ALTESSE project, *Eur. Phys. Lett.* **126**, 24001 (2019).
- [3] F. Novelli, B. Guchhait, and M. Havenith, Towards intense THz spectroscopy on water: Characterization of optical rectification by GaP, OH1, and DSTMS at OPA wavelengths, *Materials* **13**, 1311 (2020).
- [4] X. Li, T. Qiu, J. Zhang, E. Baldini, J. Lu, A. M. Rappe, and K. A. Nelson, Terahertz field-induced ferroelectricity in quantum paraelectric SrTiO₃, *Science* **364**, 1079 (2019).
- [5] A. Vella, J. Houard, L. Arnoldi, M. Tang, M. Boudant, A. Ayoub, A. Normand, G. Da Costa, and A. Hideur, High-resolution terahertz-driven atom probe tomography, *Sci. Adv.* **7**, eabd7259 (2021).
- [6] K. L. Yeh, M. C. Hoffmann, J. Hebling, and K. A. Nelson, Generation of $10 \mu\text{J}$ ultrashort THz pulses by optical rectification, *Nat. Photonics* **90**, 171121 (2007).
- [7] K. Y. Kim, A. J. Taylor, J. H. Glowina, and G. Rodriguez, Coherent control of terahertz supercontinuum generation in ultrafast laser-gas interactions, *Nat. Photonics* **2**, 605 (2008).
- [8] A. Nguyen, P. Gonz alez de Alaiza Mart inez, I. Thiele, S. Skupin, and L. Berg e, Broadband terahertz radiation from two-color mid- and far-infrared laser filaments in air, *Phys. Rev. A* **97**, 063839 (2018).
- [9] A. D. Koulouklidis, C. Gollner, V. Shumakova, V. Y. Fedorov, A. Pug zlys, A. Baltu ska, and S. Tzortzakis, Observation of extremely efficient terahertz generation from mid-infrared two-color laser filaments, *Nat. Commun.* **11**, 292 (2020).
- [10] W. P. Leemans, C. G. R. Geddes, J. Faure, C. T oth, J. van Tilborg, C. B. Schroeder, E. Esarey, G. Fubiani, D. Auerbach, B. Marcellis, M. A. Carnahan, R. A. Kaindl, J. Byrd, and M. C. Martin, Observation of Terahertz Emission from a Laser-Plasma Accelerated Electron Bunch Crossing a Plasma-Vacuum Boundary, *Phys. Rev. Lett.* **91**, 074802 (2003).
- [11] J. D echard, A. Debayle, X. Davoine, L. Gremillet, and L. Berg e, Terahertz Pulse Generation in Underdense Relativistic Plasmas: From Photoionization-Induced Radiation to Coherent Transition Radiation, *Phys. Rev. Lett.* **120**, 144801 (2018).
- [12] G.-Q. Liao, Y.-T. Li, Y.-H. Zhang, H. Liu, X.-L. Ge, S. Yang, W.-Q. Wei, X.-H. Yuan, Y.-Q. Deng, B.-J. Zhu, Z. Zhang, W.-M. Wang, Z.-M. Sheng, L.-M. Chen, X. Lu, J.-L. Ma, X. Wang, and J. Zhang, Demonstration of Coherent Terahertz Transition Radiation from Relativistic Laser-Solid Interactions, *Phys. Rev. Lett.* **116**, 205003 (2016).
- [13] J. D echard, X. Davoine, L. Gremillet, and L. Berg e, Terahertz emission from submicron solid targets irradiated by ultraintense femtosecond laser pulses, *Phys. Plasmas* **27**, 093105 (2020).
- [14] J. Yoshii, C. H. Lai, T. Katsouleas, C. Joshi, and W. B. Mori, Radiation from Cerenkov Wakes in a Magnetized Plasma, *Phys. Rev. Lett.* **79**, 4194 (1997).
- [15] C. S. Liu and V. K. Tripathi, Tunable terahertz radiation from a tunnel ionized magnetized plasma cylinder, *J. Appl. Phys.* **105**, 013313-013313-5 (2009).
- [16] W. M. Wang, P. Gibbon, Z. M. Sheng, and Y. T. Li, Tunable Circularly Polarized Terahertz Radiation from Magnetized Gas Plasma, *Phys. Rev. Lett.* **114**, 253901 (2015).
- [17] J. Sims, A. Baca, G. Boebinger, H. Boenig, H. Coe, K. Kihara, M. Manzo, C. Mielke, J. Schillig, Y. Eyssa, B. Lesch, L. Li, and H. Schneider-Muntau, First 100 T non-destructive magnet, *IEEE Trans. Appl. Supercond.* **10**, 510 (2000).
- [18] J. Singleton, C. H. Mielke, A. Migliori, G. S. Boebinger, and A. H. Lacerda, The National High Magnetic Field Laboratory Pulsed-Field Facility at Los Alamos National Laboratory, *Physica (Amsterdam)* **346B**, 614 (2004).
- [19] S. Zherlitsyn, A. D. Bianchi, T. Herrmannsdoerfer, F. Pobell, Y. Skourski, A. Sytcheva, S. Zvyagin, and J. Wosnitza, Coil design for non-destructive pulsed-field magnets targeting 100 T, *IEEE Trans. Appl. Supercond.* **16**, 1660 (2006).
- [20] S. Takeyama and E. Kojima, A copper-lined magnet coil with maximum field of 700 T for electromagnetic flux compression, *J. Phys. D* **44**, 425003 (2011).
- [21] D. Nakamura, A. Ikeda, H. Sawabe, Y. H. Matsuda, and S. Takeyama, Record indoor magnetic field of 1200 T generated by electromagnetic flux-compression, *Rev. Sci. Instrum.* **89**, 095106 (2018).

- [22] S. Fujioka, Z. Zhang, K. Ishihara, K. Shigemori, Y. Hironaka, T. Johzaki, A. Sunahara, N. Yamamoto, H. Nakashima, T. Watanabe, H. Shiraga, H. Nishimura, and H. Azechi, Kilotesla magnetic field due to a capacitor-coil target driven by high power laser, *Sci. Rep.* **3**, 1170 (2013).
- [23] J. J. Santos *et al.*, Laser-driven platform for generation and characterization of strong quasi-static magnetic fields, *New J. Phys.* **17**, 083051 (2015).
- [24] P. Sharma, N. Wadhvani, and P. Jha, Terahertz radiation generation by propagation of circularly polarized laser pulses in axially magnetized plasma, *Phys. Plasmas* **24**, 013102 (2017).
- [25] A. Saroch and P. Jha, Simulation study of terahertz radiation generation by circularly polarized laser pulses propagating in axially magnetized plasma, *Phys. Plasmas* **24**, 124506 (2017).
- [26] X.-Y. Gu, J.-S. Liu, Z.-G. Yang, S.-L. Wang, and K.-J. Wang, Theoretical investigation of tunable polarized broadband terahertz radiation from magnetized gas plasma, *Chin. Phys. B* **27**, 058701 (2018).
- [27] S. S. Ghaffari-Oskooei and F. M. Aghamir, Terahertz generation in magnetized plasma by irradiation of two-color lasers, *Phys. Plasmas* **26**, 033108 (2019).
- [28] A. V. Bogatskaya, N. E. Gnezdovskaia, and A. M. Popov, Circularly polarized terahertz pulse generation in a plasma channel created by a uv high-intense laser pulse in the presence of a static magnetic field, *Phys. Rev. E* **102**, 043202 (2020).
- [29] G. Brodin and J. Lundberg, Excitation of electromagnetic wake fields in a magnetized plasma, *Phys. Rev. E* **57**, 7041 (1998).
- [30] N. Spence, T. Katsouleas, P. Muggli, W. B. Mori, and R. Hemker, Simulations of Cerenkov wake radiation sources, *Phys. Plasmas* **8**, 4995 (2001).
- [31] N. Yugami, T. Higashiguchi, H. Gao, S. Sakai, K. Takahashi, H. Ito, Y. Nishida, and T. Katsouleas, Experimental Observation of Radiation from Cherenkov Wakes in a Magnetized Plasma, *Phys. Rev. Lett.* **89**, 065003 (2002).
- [32] Z. Hu, Z. Sheng, W. Ding, W. Wang, Q. Dong, and J. Zhang, Electromagnetic emission from laser wakefields in magnetized underdense plasmas, *Plasma Sci. Technol.* **14**, 874 (2012).
- [33] Z. D. Hu, Z. M. Sheng, W. M. Wang, L. M. Chen, Y. T. Li, and J. Zhang, Probing the laser wakefield in underdense plasmas by induced terahertz emission, *Phys. Plasmas* **20**, 080702 (2013).
- [34] F. F. Chen, *Introduction to Plasma Physics and Controlled Fusion*, 3rd ed. (Springer, Cham, Switzerland, 2016).
- [35] See Supplemental Material at <http://link.aps.org/supplemental/10.1103/PhysRevLett.128.174802> for complementary results on power loss through axial plasma gradients, higher conversion efficiencies through longer plasmas and details on lateral THz emissions from transverse plasma gradients, which includes Refs. [36,37].
- [36] P. González de Alaiza Martínez, X. Davoine, A. Debayle, L. Gremillet, and L. Bergé, Terahertz radiation driven by two-color laser pulses at near-relativistic intensities: Competition between photoionization and wakefield effects, *Sci. Rep.* **6**, 26743 (2016).
- [37] E. Esarey, C. B. Schroeder, and W. P. Leemans, Physics of laser-driven plasma-based electron accelerators, *Rev. Mod. Phys.* **81**, 1229 (2009).
- [38] A. Holkundkar, G. Brodin, and M. Marklund, Wakefield generation in magnetized plasmas, *Phys. Rev. E* **84**, 036409 (2011).
- [39] E. Lefebvre, N. Cochet, S. Fritzier, V. Malka, M. M. Aléonard, J. F. Chemin, S. Darbon, L. Disdier, J. Faure, A. Fedotoff, O. Landoas, G. Malka, V. Méot, P. Morel, M. Rabec LeGloahec, A. Rouyer, C. Rubbelynck, V. Tikhonchuk, R. Wrobel, P. Audebert, and C. Rousseaux, Electron and photon production from relativistic laser plasma interactions, *Nucl. Fusion* **43**, 629 (2003).
- [40] R. Nuter, L. Gremillet, E. Lefebvre, A. Lévy, T. Ceccotti, and P. Martin, Field ionization model implemented in Particle In Cell code and applied to laser-accelerated carbon ions, *Phys. Plasmas* **18**, 033107 (2011).
- [41] W. Lu, M. Tzoufras, C. Joshi, F. S. Tsung, W. B. Mori, J. Vieira, R. A. Fonseca, and L. O. Silva, Generating multi-GeV electron bunches using single stage laser wakefield acceleration in a 3D nonlinear regime, *Phys. Rev. ST Accel. Beams* **10**, 061301 (2007).
- [42] J. Vieira, J. L. Martins, V. B. Pathak, R. A. Fonseca, W. B. Mori, and L. O. Silva, Magnetically assisted self-injection and radiation generation for plasma-based acceleration, *Plasma Phys. Controlled Fusion* **54**, 124044 (2012).
- [43] Equation (1) was originally derived in Ref. [32] for an external B field aligned with the laser's electric field ($\vec{a}_0 \parallel \vec{B}_0 \parallel \vec{e}_z$) rather than normal to it ($\vec{B}_0 \parallel \vec{e}_y$), as considered in our simulations. In the Supplemental Material [35] it is demonstrated that the low-frequency wakefield components still obey Eq. (1) under our conditions.